PHYSICAL REVIEW E **94**, 023204 (2016)

Dissociation along the principal Hugoniot of the Laser Mégajoule ablator material

P. Colin-Lalu,[1,2] V. Recoules,[1] G. Salin,[1] T. Plisson,[1] E. Brambrink,[2] T. Vinci,[2] R. Bolis,[2] and G. Huser[1,*]

[1]*CEA, DAM, DIF, Bruyères-le-Châtel, F-91297 Arpajon, France*

[2]*Laboratoire pour l'Utilisation des Lasers Intenses (LULI) - CEA, CNRS, Ecole Polytechnique : Université Paris-Saclay, UPMC Université Paris 06 : Sorbonne Universités - F-91128 Palaiseau, France*

(Received 27 May 2016; published 16 August 2016)

Glow discharge polymer hydrocarbon (GDP-CH) is used as the ablator material in inertial confinement fusion (ICF) capsules for the Laser Mégajoule and National Ignition Facility. Due to its fabrication process, GDP-CH chemical composition and structure differ from commercially available plastics and detailed knowledge of its properties in the warm dense matter regime is needed to achieve accurate design of ICF capsules. First-principles *ab initio* simulations of the GDP-CH principal Hugoniot up to 8 Mbar were performed using the quantum molecular dynamics (QMD) code ABINIT and showed that atomic bond dissociation has an effect on the compressibility. Results from these simulations are used to parametrize a quantum semiempirical model in order to generate a tabulated equation of state that includes dissociation. Hugoniot measurements obtained from an experiment conducted at the LULI2000 laser facility confirm QMD simulations as well as EOS modeling. We conclude by showing the EOS model influence on shock timing in a hydrodynamic simulation.

DOI: 10.1103/PhysRevE.94.023204

I. INTRODUCTION

Inertial confinement fusion (ICF) experiments on large laser facilities aim at imploding a spherical capsule made of an ablator material and filled with a deuterium-tritium (D-T) mixture in cryogenic and gaseous form. The spherical implosion creates a hot spot at the center of the capsule, where density and temperature are expected to become high enough to trigger thermonuclear reactions and subsequent α heating of the surrounding cryogenic fuel. Recent experiments at the National Ignition Facility (NIF) have shown that fuel gain by α heating was obtained [1] using adiabat shaping of the laser pulse in order to reduce hydrodynamic instabilities during implosion. While these results are very encouraging for the success of ICF using megajoule-scale laser facilities, interpretations of ICF experiments by numerical simulations are still subject to various empirical adjustments because of insufficiencies in the description of underlying physics such as transport coefficients and the equation of state (EOS).

Triggering thermonuclear fusion at the center of the capsule translates into high implosion velocities ($\sim$370 km/s) [2] for which a low-density ($\sim$1 g/cm^3) ablator such as plastic is suitable. To reach these conditions, the ablator material is subjected to a sequence of shocks and its thermodynamic path crosses the so-called warm dense matter (WDM) region of the temperature-density (T-ρ) phase diagram ($T \sim$ 1–100 eV, $\rho \sim 0.01\rho_0$–$10\rho_0$) in which matter is found in the form of a weakly ionized, strongly coupled, partially degenerate plasma. Because of its transient nature between a cold solid and an ideal plasma, the WDM description remains a daunting task and hydrodynamic simulation tools rely on tabulated EOSs such as QEOS [3] or SESAME [4] which provide thermodynamics properties of materials over several decades in density and temperature by combining various models. Each of these models was validated in limited regions of the phase diagram, but none of them provide an accurate description of WDM, which is described by means of interpolations and empirical correction terms.

To improve tabulated EOS models of ablator materials, efforts have been concentrated on experiments and quantum molecular dynamics (QMD) simulations. Until recent years, most studies on the EOS of the plastic ablator focused on idealized CH mixtures for calculations [5–11] and polystyrene or polyethylene for experiments [12–15]. However, spherical capsules used for ICF experiments cannot be fabricated using commercially available CH polymers. During the fabrication process, CH is deposited on a foam mandrel (dissolved thereafter by pyrolysis) using glow discharge polymerization (GDP). This process produces an amorphous structure and oxygen from ambient air humidity is then introduced in the bulk upon storage. The structure of GDP-CH was examined by conducting x-ray diffraction measurements of GDP-CH samples in a diamond anvil cell (DAC) using the ESRF synchrotron facility [16]. These measurements confirmed the amorphous structure and absence of recrystallization of GDP-CH up to at least 20 GPa. The atomic fraction of oxygen in GDP-CH has also been the subject of recent investigations and it has been shown that its uptake was due to ambient humidity [17]. Huang *et al.* [18] measured an atomic fraction of oxygen reaching up to 5% in General Atomics GDP-CH using contact radiography. The oxygen atomic fraction in CH-GDP fabricated at the CEA target group was also analyzed. Crossed analyses of Rutherford backscattering spectroscopy on thin samples ($\sim$100 nm) and infrared spectroscopy under nitrogen atmosphere pyrolysis of massive samples (thickness $\sim$ mm) led to an average oxygen atomic fraction of 3%. Furthermore, infrared spectroscopy measurements of GDP-CH samples in ambient conditions showed the presence of C-O bonds, supporting the fact that oxygen is integrated into the bulk and not just adsorbed on the surface.

These refinements in the description of the ablator material were motivated by the need for a better knowledge of the ablator EOS that would include precise chemical composition and behavior, because this has a direct influence on shock timing [19,20] as well as growth of hydrodynamic instabilities

*gael.huser@cea.fr

[21,22]. Recent studies in the WDM region of the phase diagram have been performed in that direction with experiments on actual NIF capsule ablator materials [23] and first-principles calculations of the $CH_{1.36}$ mixture which is a related capsule material [24].

In the WDM regime, shock states described by the Hugoniot curve are affected by dissociation. A detailed description of dissociation in shocked polyethylene was provided in Ref. [5] but limited to pressures ∼3.5 Mbar. An extended study of the phase diagram of polystyrene using QMD and OFMD (orbital free molecular dynamics) was performed in Refs. [9,11], but does not give a detailed description of dissociation. In the continuation of these studies, this work is dedicated to further improvement in the description of GDP-CH in the WDM regime. We present QMD Hugoniot calculations of CHO mixtures with atomic proportions relevant to the chemical composition of GDP-CH. These calculations were performed up to ∼8 Mbar in order to obtain a detailed description of dissociation. We find that compressibility of GDP-CH up to ∼5 Mbar is higher than that predicted by average atom modeling because of dissociation of C-C and C-H bonds. The QMD results are then used to generate an EOS model. Reference [24] also provides an EOS table adjusted on QMD calculations, but it uses calculations in the liquid state and solid state properties are extrapolated. Here, we present a quantum semiempirical EOS model that takes into account the effect of dissociation along the Hugoniot. We then present results obtained during a laser-shock experiment at the LULI2000 facility that confirm QMD calculations and EOS modeling. Finally, we use our proposed EOS model to estimate the influence on shock timing predictions in conditions related to ICF.

II. EQUATION OF STATE MODELING

A. Quantum molecular dynamics

GDP-CH Hugoniot states up to 8 Mbar were calculated using quantum molecular dynamics. Simulations are performed using the *ab initio* plane wave density functional theory (DFT) code ABINIT [25–27]. DFT is applied together with the generalized gradient approximation [28]. Simulations are performed in the framework of the projector augmented wave (PAW) method [29,30]. The PAW data sets are generated using 4 outer electrons ($2s^2 2p^2$) and a cutoff radius $r_c = 1.10a_B$ for carbon (where a_B is Bohr radius), and using 6 outer electrons ($2s^2 2p^4$) and a cutoff radius $r_c = 1.20a_B$ for oxygen. The cutoff radius for hydrogen is $r_c = 0.80a_B$. These PAW data sets were tested at up to 9 g/cm^3 and 40 eV temperature [6]. We use a plane wave basis with an energy cutoff set at 30 Ha (816.34 eV) in order to converge pressure and energy calculations. The cubic simulation box includes 250 atoms: 102 C, 140 H, and 8 O in order to reproduce the GDP-CH measured stoichiometry. The number of atoms is limited by available machine time and was considered to be sufficiently high by comparing to previous similar QMD studies which used 125 and up to 236 atoms (Refs. [9,24], respectively).

To simulate CHO mixtures representative of GDP-CH at a given thermodynamic state, quantum molecular dynamics (QMD) simulations are performed at the Γ point for representation of the Brillouin zone. Some states were tested with a $2 \times 2 \times 2$ Monkhorst-Pack k-point sampling and differences in pressures were found to be below 1.4%. At each ionic time step, forces are computed within DFT using the Hellman-Feynman theorem. We assume thermodynamic equilibrium with ionic temperature equal to the electronic temperature. The electron temperature is controlled by the width of the Fermi-Dirac distribution. The ion temperature is controlled and maintained in the isokinetics ensemble where the velocities are rescaled at every time step. Before reaching a stable ion structure, the system relaxes for a few hundred time steps. After equilibration, pressure fluctuates around a well-defined value and thermodynamic parameters can be obtained by statistical averaging.

The Hugoniot curve is given by Rankine-Hugoniot energy conservation

$$E_1 - E_0 = \frac{1}{2}(P_1 + P_0)\left(\frac{1}{\rho_0} - \frac{1}{\rho_1}\right), \tag{1}$$

where E is internal energy, P is pressure, ρ is shock density, and initial and shocked states are indexed 0 and 1, respectively. To find a Hugoniot point, we first calculate an isochore and then determine by interpolation the temperature that satisfies Eq. (1). Isochores where calculated in a region where we expected to find the Hugoniot curve, for densities ranging from 2.4 to 3.4 g/cm^{-3} and temperatures ranging from 0.25 to 6 eV (Fig. 1). The initial internal energy E_0 and atomic configurations were taken from GDP-CH cold curve calculations [31].

Hugoniot states determined using QMD are given in Table I and also include shock and fluid velocities U_s and u_p defined by $U_s = \sqrt{[\rho_1(P_1 - P_0)]/[\rho_0(\rho_1 - \rho_0)]}$ and $u_p = U_s(1 - \rho_0/\rho_1)$. From the determined Hugoniot conditions, a

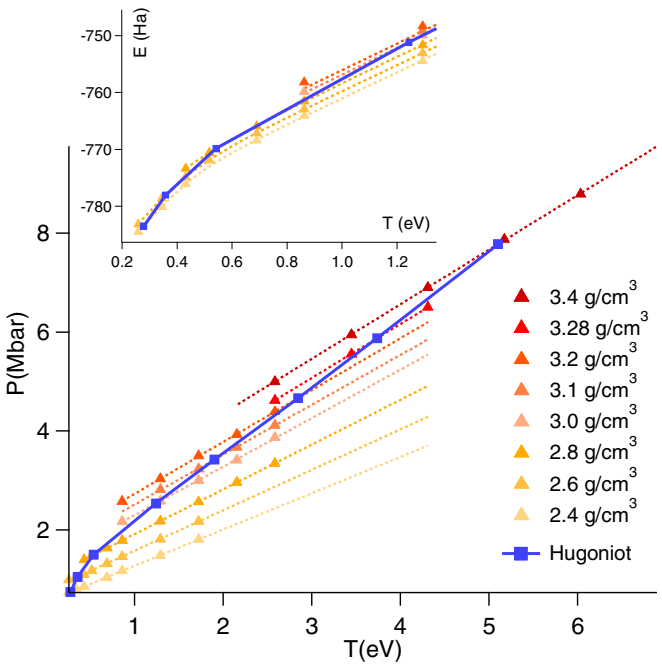

FIG. 1. GDP-CH isochores calculated using QMD simulations. The inset shows a close-up of isochores in the energy-temperature plane. Dotted lines are fits to guide the eye.

TABLE I. Hugoniot states simulated using QMD.

ρ (g/cm^3)	T (eV)	P (Mbar)	u_p (km/s)	U_s (km/s)	ρ/ρ_0
2.4	0.28	0.74	6.21	11.20	2.24
2.6	0.36	1.05	7.60	12.92	2.43
2.8	0.54	1.50	9.30	15.06	2.62
3	1.24	2.53	12.34	19.19	2.80
3.1	1.90	4.66	14.47	22.1	2.90
3.2	2.85	4.66	17.03	25.59	2.99
3.28	3.74	5.87	19.23	28.55	3.07
3.4	5.10	7.78	22.32	32.57	3.18

second set of QMD calculations was executed in order to study the structural properties of shock compressed GDP-CH. For the lowest simulated Hugoniot state, the pair correlation function for carbon atoms $g_{\text{C-C}}(r)$ shows a prominent peak around radius $r = 1.5$ Å (Fig. 2), in close agreement with values for C-C bonds lengths found in chemical handbooks. We therefore associate this peak with chemical bonding between carbon atoms. Similar features are seen in C-H and H-H pair correlation functions and GDP-CH can be described as a molecular liquid. When Hugoniot density and temperature increase, C-C bonds vanish for ($\rho \approx 3$ g/cm^3, $T \approx 1.28$ eV) and a simple dissociated liquid is described. Vanishing of H-H and C-H bonds is observed at lower densities and temperatures, respectively ($\rho \approx 2.6$ g/cm^3, $T \approx 0.36$ eV) and ($\rho \approx 2.8$ g/cm^3, $T \approx 0.56$ eV). The effect of dissociation is also visible in the energy isochores depicted in the inset of Fig. 1: for temperatures below ~0.5 eV, the presence of bonds causes the curves to bend, whereas these are linear when bonds vanish at higher temperatures.

B. Analytical modeling

To include the effects of GDP-CH dissociation in hydrodynamic simulations we generated an equation of state table using a quantum semiempirical model (QSEM). The QSEM construction is similar to the quotidian equation of state (QEOS) model [3], where ion and electron pressure are calculated separately. Both QEOS and QSEM models are so-called average-atom models. The main differences between these two models are in the description of the electron EOS and

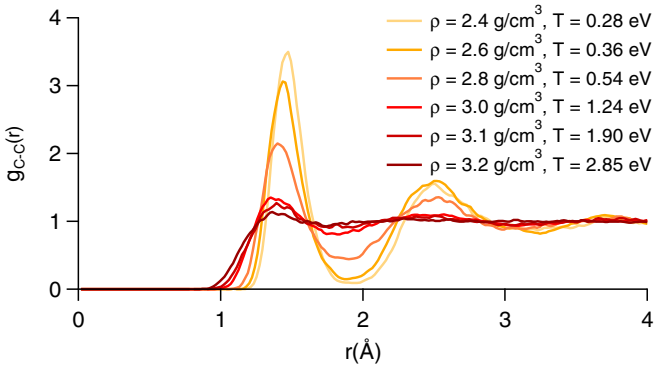

FIG. 2. C-C pair correlation function for GDP-CH along simulated Hugoniot states.

of the 300 K isotherm (sometimes referred as cold curve). In the QEOS model, the electron EOS is given by Thomas-Fermi theory which allows atomic weight A and number Z scaling as well as mixture EOS using an isobaric mixing rule. In the QSEM, the electron EOS is based on a fully quantum calculation where each element is tabulated using the VAAQP code (variational average atom in quantum plasmas) [32] with the Inferno [33] option. In QEOS, the cold curve is obtained by applying a chemical bond correction [34] on the electron pressure. In QSEM, the 300 K isotherm is provided externally by a solid state physics model and/or experimental data. In the case of GDP-CH, we use a cold curve previously calculated by QMD [31] and validated up to 0.5 Mbar using static compression in a diamond anvil cell [16].

Common to both average atom QEOS and QSEM models is the Cowan ion EOS [3] which depends explicitly on A and Z as well as on the Grüneisen parameter Γ. Formally speaking, the Grüneisen parameter is an arbitrary function of specific volume V, arising from the integration of thermodynamic consistency $(\partial E/\partial V)_T = T(\partial p/\partial T)_V - P$. A macroscopic (or thermodynamic) definition is then given by the Mie-Grüneisen EOS $\Gamma(V) = V(\partial P_{th}/\partial E_{th})_V$, where P_{th} and E_{th} are the thermal components of ion pressure and energy [35].

The Cowan ion EOS uses the Debye model to describe the solid phase, in which harmonic vibrations of the atoms around their equilibrium positions are assumed, allowing free energy F to be written as $F = E_c(V) + 3Nk_BT\ln(h\bar{\nu}/k_BT)$, where E_c is the potential energy (or elastic component of the internal energy), N is the number of atomic nuclei, and $\bar{\nu}$ is the average frequency of the phonon spectrum. By deriving total pressure and internal energy from the free energy, a microscopic definition of the Grüneisen parameter is obtained: $\Gamma(V) = -\partial\ln\bar{\nu}/\partial\ln V$. This definition has more physical meaning, since Γ is now directly linked to the vibration spectrum via the average frequency $\bar{\nu}$, and can be seen as expressing the vibrational response of the lattice to thermal excitation. One way to include dissociation in an average atom EOS model is thus to give an explicit density dependence to the Grüneisen parameter. This calculation can be straightforward within the harmonic approximation in which the vibrational spectrum follows a parabolic dependency ν^2. The true knowledge of this spectrum depends on the lattice structure and is usually much more complex. The vibrational spectrum can be accessed using dedicated experiments such as neutron scattering [36], but these are not feasible at Mbar pressures. Calculation of the vibrational spectrum using QMD simulations is in principle feasible but must be performed on a periodic crystalline structure [37], which does not apply to the case of amorphous CH-GDP. Our cold curve and Hugoniot simulations however provide statistically averaged total energy and pressures. The thermal components of the EOS can then be obtained from the subtraction of Hugoniot and cold curve. This allows us to rewrite the Mie-Grüneisen EOS as a function of cold pressure $P_c(\rho)$ and Hugoniot calculations $P_H(\rho)$ using

$$\Gamma(\rho) = \frac{1}{\rho}\frac{P_H(\rho) - P_c(\rho)}{\left\{\frac{1}{2}[P_H(\rho) + P_0]\left(\frac{1}{\rho} - \frac{1}{\rho_0}\right) - \int_{\rho_0}^{\rho} P_c(\rho')/\rho'^2 d\rho'\right\}}, \tag{2}$$

where 0 refers to normal conditions and where the integral is the cold curve contribution to total energy.

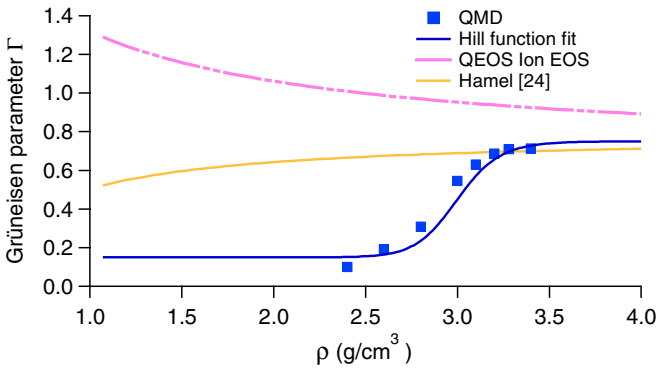

FIG. 3. GDP-CH Grüneisen parameter deduced from cold curve and Hugoniot QMD calculations (blue filled squares) is fitted using a Hill function (continuous blue line) to produce an effective Γ, and compared with QEOS ion EOS (dashed pink line) and Hamel [24] $CH_{1.36}$ EOS (orange line).

The Grüneisen parameter calculated according to Eq. (2) is close to 0.1 for the lowest simulated density, increases, and asymptotes to ∼0.72 when the fluid is completely dissociated (Fig. 3). To include this modified Γ into the ion EOS, the QMD determined values can be represented using a Hill function to express an effective Grüneisen parameter:

$$\Gamma_{\text{eff}}(\rho) = x_{\min} + \frac{x_{\max} - x_{\min}}{1 + \left(\frac{x_1}{\rho}\right)^n}, \tag{3}$$

where $x_{\min}$, $x_{\max}$, x_1, and n are numerical parameters. To ensure thermodynamic consistency, these parameters are also used to express Debye temperature Θ_D and melting temperature T_m, given by

$$\Theta_D(\rho) = \Theta_{D,0}\left(\frac{\rho}{\rho_0}\right)^{x_{\min}}\left(\frac{\rho^n - x_1^n}{\rho_0^n - x_1^n}\right)^{(x_{\max}-x_{\min})/n}, \tag{4}$$

$$T_m(\rho) = T_{m,0}\left(\frac{\rho}{\rho_0}\right)^{2x_{\min}-2/3}\left(\frac{\rho^n - x_1^n}{\rho_0^n - x_1^n}\right)^{2(x_{\max}-x_{\min})/n}, \tag{5}$$

where index 0 refers to normal conditions.

The effective Grüneisen parameter Γ_{eff} is reinjected into the Cowan ion EOS in order to produce a Hugoniot curve that passes through the QMD Hugoniot data. The Γ which is given by Eq. (2) by definition includes contributions accounting for thermal excitation of both ions and electrons. These electronic thermal contributions must therefore be subtracted from Eq. (2) when reinjecting into the ion EOS model. This is done iteratively and the set of numerical parameters ($x_{\min}$, $x_{\max}$, x_1, n) which produces a total pressure in agreement with QMD pressure is (0.15, 0.75, 3, 26). This procedure produces an effective Γ which is shifted 2%–3% to higher densities compared to QMD Γ calculated using Eq. (2). This shift reflects electronic thermal contributions.

Modifying the QEOS model has already been done in the past, such as in Ref. [38], which includes the possibility of arbitrary modification of the Grüneisen parameter in order to better match experimental data. Here, we also modify the Grüneisen parameter, but modifications are constrained by the QMD Hugoniot and cold curve. Comparison with experimental data will be made in the next section to validate our modeling.

When comparing our effective Γ to the one used in the original QEOS model, we find a very different behavior: the Grüneisen parameter in QEOS decreases with Hugoniot density whereas in our modeling, the effective Γ transitions from 0.15 at low densities to a 0.75 value. Our effective Γ is in better agreement with the Grüneisen parameter from the Hamel [24] $CH_{1.36}$ EOS which also increases as function of density. However, the Hamel EOS is a wide-ranging Mie-Grüneisen EOS fitted onto liquid-state QMD simulations in which energy isochores were fitted linearly and thus does not consider dissociation. Additional constraints on the representation of the effective Γ by a Hill function could be obtained using supplementary QMD calculations at below and beyond the explored density range. This is however not critical since the Hugoniot curve differs little from the cold curve for densities below 2.5 g/cm^3 (see Fig. 4), which means that thermal components of the EOS can be neglected. For the highest explored densities, dissociation is complete and the effective Γ reaches 0.75 (close to the perfect gas limit 2/3) when dissociation is complete.

GDP-CH Hugoniot curves extracted from the QSEM with the effective Γ are presented in Fig. 4 in the pressure-compression and temperature-compression planes and are compared to existing models and previous works on similar plastic materials. Focus is given to the 0–100 Mbar pressure range which is most relevant to the ablator thermodynamical path during the implosion of ICF capsules. In this region, the most striking feature of the QSEM compared to QEOS is the increased relative compressibility in the 0.5–10 Mbar pressure range. LEOS5350 or the Hamel [24] $CH_{1.36}$ EOS also predict higher compressibilities compared to QEOS, but the available Hugoniot curves from these models do not show a clear indication of dissociation. Note that according to Ref. [24], LEOS 5350 does include dissociation following Ref. [38]. This model allows inclusion of dissociation empirically, using fitting coefficients. In our case, dissociation is described through an effective Γ, which expression is fitted on QMD with no further correction. Interestingly, even though the QSEM is parametrized using QMD simulations on a restricted range of the phase diagram, the extracted Hugoniot extrapolates well to lower pressures (studied in more detail in Ref. [5]) as well as to high pressures [9,11].

III. HUGONIOT MEASUREMENTS

To validate our modeling, we produced GDP-CH Hugoniot data obtained during an experiment conducted at the LULI2000 laser facility. Pressure-density Hugoniot states in GDP-CH were measured using the impedance mismatch (IM) technique with aluminium (Al) as the reference material. In the IM technique, the Hugoniot state in the sample of interest is determined from conservation of pressure and fluid velocity at transmission of a shock from a reference material (e.g., which EOS is considered to be known with reasonable accuracy). In our experiments, we measured the release from Al into less dense GDP-CH. In order to perform IM, one needs to determine shock speeds in Al and GDP-CH at the interface between both materials. The incident shock state in

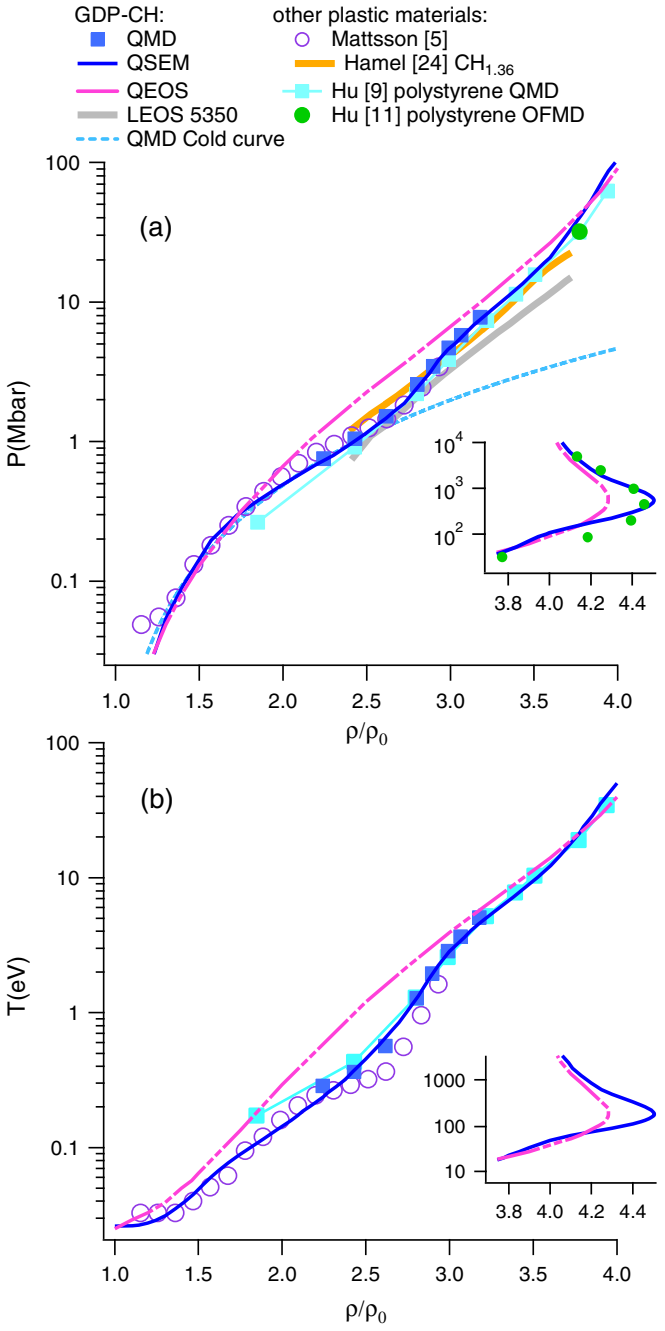

FIG. 4. GDP-CH Hugoniot in (a) pressure-compression plane and (b) temperature-compression plane. The QSEM (blue line) fitted to QMD calculations (blue filled squares) is compared to QEOS (pink dashed line) and LEOS5350 (gray line, taken from Ref. [24]). Other plastic materials are also shown: QMD calculations on polyethylene [5] (purple open circles) and polystyrene [9] (cyan line and filled squares), and Mie-Grüneisen EOS fitted on QMD calculations for $CH_{1.36}$ mixtures [24] (orange line). Insets show high pressure and temperature region of the Hugoniot, with the same units as in the main graphs. Green filled circles in top graph are high-temperature orbital free molecular dynamics calculations from Ref. [11]. Also shown in blue dashed line in panel (a) is the QMD cold curve from Ref. [31].

Al is represented in the pressure-fluid velocity plane (P,u_p) by the intersection of the Rayleigh line (which equation

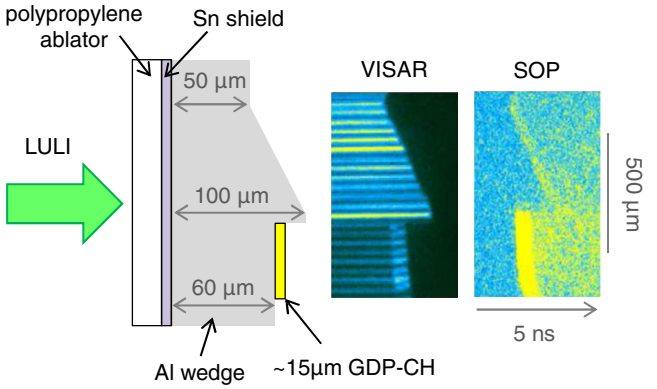

FIG. 5. Experimental configuration and corresponding VISAR and SOP images, with identical time and space scales.

$P^{\mathrm{Al}} = \rho_0^{\mathrm{Al}} U_s^{\mathrm{Al}} u_p$ is determined by the observable U_s^{Al}) with the Al Hugoniot. When the shock is transmitted into GDP-CH, shock velocity U_s^{GDP} can be measured and the shock state in GDP-CH is given by the intersection of the Al release isentrope and GDP-CH Rayleigh line $P^{\mathrm{GDP}} = \rho_0^{\mathrm{GDP}} U_s^{\mathrm{GDP}} u_p$.

The Al reference Hugoniot EOS was determined using gas-gun, underground nuclear explosions, as well as the Z-pinch facility, and data were compiled in a single fit in Ref. [39]. The Al release isentrope can be calculated using a Mie-Grüneisen EOS, expressing $\Gamma = V(\frac{\partial P}{\partial E})_V$. For sufficiently high shock temperatures, Al can be considered to be a monoatomic liquid and Γ can be taken as a constant close to the ideal gas value 2/3. In order to gain more accuracy, we used a recent work by Knudson *et al.* [40] which brings a more refined approach using an analytical model adjusted on first-principles calculations of Al release and validated with experiments using low-impedance aerogel standards. This framework uses an effective Hugoniot slope and Grüneisen coefficient, both depending on shocked Al fluid velocity only.

High-pressure shocks were generated using the LULI2000 laser facility at Ecole Polytechnique which delivers energy in two double-frequency laser beams at 527 nm. Laser energy was varied from 250 to 900 J and was contained into a 1.5 ns square pulse focused onto a 1 mm focal spot using hybrid phase plates. Targets for the study of GDP-CH consisted of several layers (Fig. 5). A ~30 μm thick polypropylene-CH ablator material, coated with 0.1 μm of aluminum (Al) to avoid laser shine-through, was used as the ablator material. The low atomic number of this material reduces production of hard x rays in the coronal plasma. An additional x-ray shield consisting of 2.5 μm of tin (Sn) was also added. Tin was chosen because of its high atomic number ($Z = 50$) and relatively low density (7.3 g/cm^3) minimizing shock reflection phenomena. The pusher was aluminium, machined into a wedge-shaped step, allowing measurement of shock speed and control of its steadiness. The GDP-CH sample was glued using polyvinyl alcohol next to the upper part of the Al step. Glue thickness using this technique was kept below 1–2 μm.

When the laser beams irradiate the front surface of the target, an ablation front is produced which pushes ahead a shock front that is transmitted into the Al layer. When the shock is transmitted from Al to GDP-CH, its pressure is

TABLE II. Measured optical constants of GDP-CH at 532 and 1064 nm: real and imaginary parts of the index of refraction n_0 and k_0 and absorption coefficent α.

λ	n_0	k_0	α (μm^{-1})
532 nm	1.564	5.53×10^{-4}	1.31×10^{-2}
1064 nm	1.538	$<10^{-6}$	$<10^{-5}$

strong enough (1–5 Mbar depending on laser intensity) so that the shock front is reflective. Shock speeds, reflectivities, and self-emission signals were obtained using the line-imaging velocity interferometers system for any reflector (VISAR) and the self-emission optical pyrometer (SOP) coupled to streak cameras. The probe beam used for the VISAR diagnostic was generated using a Nd:YAG laser emitting a $\sim$10 ns square pulse shape at 532 and 1064 nm wavelength. A dichroic beamsplitter was used in order to have one VISAR at 532 nm and the other at 1064 nm, enabling optical measurements at both wavelengths. Fringe sensitivities in GDP-CH were 4.42 km/s/fringe for the 1064 nm VISAR and 15.74 km/s/fringe for the 532 nm VISAR. The VISAR diagnostic allows measurement of a fringe shift with 5% error using the Neutrino fringe unwrapping software [41].

GDP-CH has a dark, brownish color, making it highly absorptive to visible light and especially for VISAR measurements at 532 nm. Its index of refraction and absorption were measured using spectroscopic ellipsometry and spectrophotometry. These analyses yielded an absorption coefficient $\alpha \sim 1.5 \times 10^{-2}$ μm^{-1} at 532 nm wavelength (see Table II) which translates into $\sim$60% absorption of the 532 nm probe beam after reflection off the Al/GDP-CH interface for 15 μm GDP-CH samples. When designing this experiment, this very strong absorption cast some doubts about the feasibility of using quartz as an EOS standard, because measurement of the shock front velocity in a quartz plate placed behind the absorptive GDP-CH sample is necessary to perform IM. For that reason, we decided to use a more robust target design using an Al standard. Implementing a 1064 nm VISAR also proved to be very useful for extracting fringe shifts since GDP-CH has much higher transparency at this wavelength.

Shock speed in Al U_s^{Al} was obtained by measuring transit time between the Al/CH-GDP interface and the top of the Al step and its steadiness was controlled using wedge contour analysis. When the shock breaks out at the Al/GDP-CH interface or at the top of the step, the intensity signal does not change instantaneously but follows a ramp which temporal duration is given by the convolution of the VISAR etalon delay and the streak camera slit temporal width. This results in rise and descent times of $\sim$100 ps and $\sim$150 ps for the 532 and 1064 nm VISAR at 5 ns time windows, respectively, and approximately doubles for the 10 ns time window. Shock transit times were measured from the beginnings of the intensity rising ramp at the Al/GDP-CH interface and intensity decreasing ramp at the Al/vacuum interface.

Errors on shock speed in Al include contributions from transit time measurements ($\sim$5 pixels), step height measurements (0.3–0.5 μm), sweep speed ($\sim$2% on transit time), and shock steadiness ($\sim$2% on shock speed), all summed into quadrature,

TABLE III. Shot number, shock velocities in Al and GDP-CH used for IM technique, and corresponding Hugoniot pressure and compression in GDP-CH. Associated errors are in parentheses.

No.	U_s^{Al} (km/s)	U_s^{GDP} (km/s)	P^{GDP} (Mbar)	$(\rho/\rho_0)^{\mathrm{GDP}}$
7	16.72(0.40)	17.93(0.22)	2.20(0.13)	2.77(0.23)
9	23.09(0.50)	26.83(0.22)	5.14(0.26)	3.01(0.22)
11	20.73(0.46)	23.87(0.22)	3.95(0.21)	2.84(0.20)
12	16.81(0.37)	18.2(0.22)	2.25(0.13)	2.73(0.20)
13	16.45(0.36)	17.7(0.22)	2.11(0.12)	2.70(0.20)
14	22.64(0.51)	26.16(0.22)	4.89(0.26)	3.01(0.23)
15	16.15(0.37)	17.23(0.22)	2.00(0.12)	2.71(0.21)
19	15.63(0.35)	16.32(0.22)	1.81(0.11)	2.74(0.22)
20	14.53(0.32)	14.75(0.22)	1.46(0.09)	2.67(0.20)
23	14.44(0.32)	14.6(0.22)	1.43(0.09)	2.67(0.21)

amounting to errors slightly above $\geqslant$2% on shock speed. In this experiment, shock speeds ranged from 14 to 23 km/s with corresponding errors ranging from 0.3 to 0.5 km/s, translating into a typical 8% error on compression (see Table III).

When the shock travels in the Al step, side rarefactions occurring at the edge of the step can overtake the shock front and perturb breakout time if measurement is taken too close to the edge. This problem was first addressed in gas-gun experiments [42] where it was shown that overtaking of the shock front by lateral sound waves can be calculated using knowledge of the sound velocity and a geometric construction. In our experimental conditions, curving of the shock is expected to occur up to $\sim$10 μm away from the edge of the step, corresponding to $\sim 1/4$ fringe on the VISAR images. In order to avoid rarefaction effects, the top of the step was machined flat over 40 μm, which is equal to the height of the step, and breakout times were measured sufficiently far away from the edge.

Shock unsteadiness was estimated from contour analysis of shock breakout from the wedge. Time history of shock velocity in the wedge is given by the derivative of the extracted contour, so that a linearly varying shock would produce a parabolic trace on the streak image. Fitting the contour of the wedge was however limited to linear, as higher order fittings led to the same root-mean-square value σ of the fit residuals. In other terms, shock unsteadiness is below detection limits using this technique. An upper bound on shock unsteadiness at detection limit was evaluated by considering parabolic traces starting at t_0, passing through $t_1 \pm \sigma$, and which derivatives at t_0 are equal to the slope of the linear fit, where t_0 and t_1 are the times corresponding to shock breakout at the bottom and the top of the wedge, respectively. These inferred parabolic traces are derived to linear time evolutions of shock velocity across the wedge. Using the inferred shock velocity histories, the difference between averaged shock velocity (which is the observable) and shock velocity at the Al/GDP-CH interface is $\sim$1.5%–2% depending on the shot considered in this analysis.

Temperature of the shock front in GDP-CH was obtained by absolute pyrometry using the SOP diagnostic. Some shots were devoted to quartz targets on which shock velocity, reflectivity, and self-emission signals were recorded. Quartz reflectivity and temperature as a function of shock speed were measured

in previous works [43,44], enabling their use as a reference for calibrating the SOP system. Quartz temperature as function of SOP CCD count intensity I recorded by the SOP diagnostic was fitted by

$$T = T_0/\ln\{1 + [1 - R(I)]A/I\}, \quad (6)$$

where T_0 and A are the fit parameters and $R(I)$ is quartz reflectivity at a given count intensity. We find $T_0 = 1.83 \pm 0.09$ eV and $A = 4833 \pm 240$, where errors arise mainly from fluctuations of quartz reflectivity profiles. Using this calibration, equivalent black-body temperatures in GDP-CH can be deduced from the SOP intensity, after correction from absorption in GDP-CH. An additional correction by the measured reflectivity at 532 nm provided equivalent gray-body temperatures which were assimilated to shock temperatures. Error on shock temperature includes contributions from calibration as well as fluctuations on raw SOP intensity signal and amounts to 15%–25% depending on image signal-to-noise ratio.

Experimental data collected during the LULI experiment clearly confirms Hugoniot QMD and QSEM predictions over previous tabulated EOS (Fig. 6). Despite the error on compression, data confirm the influence of the dissociation of carbon bonds on the Hugoniot compressibility, as outlined in previous works on plastic materials [5,44]. We also note that up to 5 Mbar the LULI data is in good agreement with Omega data [23], reanalyzed following Ref. [45]. For higher pressures, the Omega data display a systematic compression shift from the QEOS model. In contrast, for pressures above 5 Mbar, both our modeling and experimental data favor a stiffer Hugoniot when dissociation is complete.

Shock temperature data [Fig. 6(b)] are also in good agreement with QMD and QSEM. It is not surprising to find temperatures below QEOS, since the presence of bonds in the measured compression range allows more heat to be absorbed by vibrational states. Interestingly, Omega polystyrene data [15], reanalyzed using the Knudson quartz release model [45], are in good agreement with our data and QSEM, whereas previous analyses of this data set using older quartz standards [24,39] displayed noticeable compression shifts [45], leading to discrepancies.

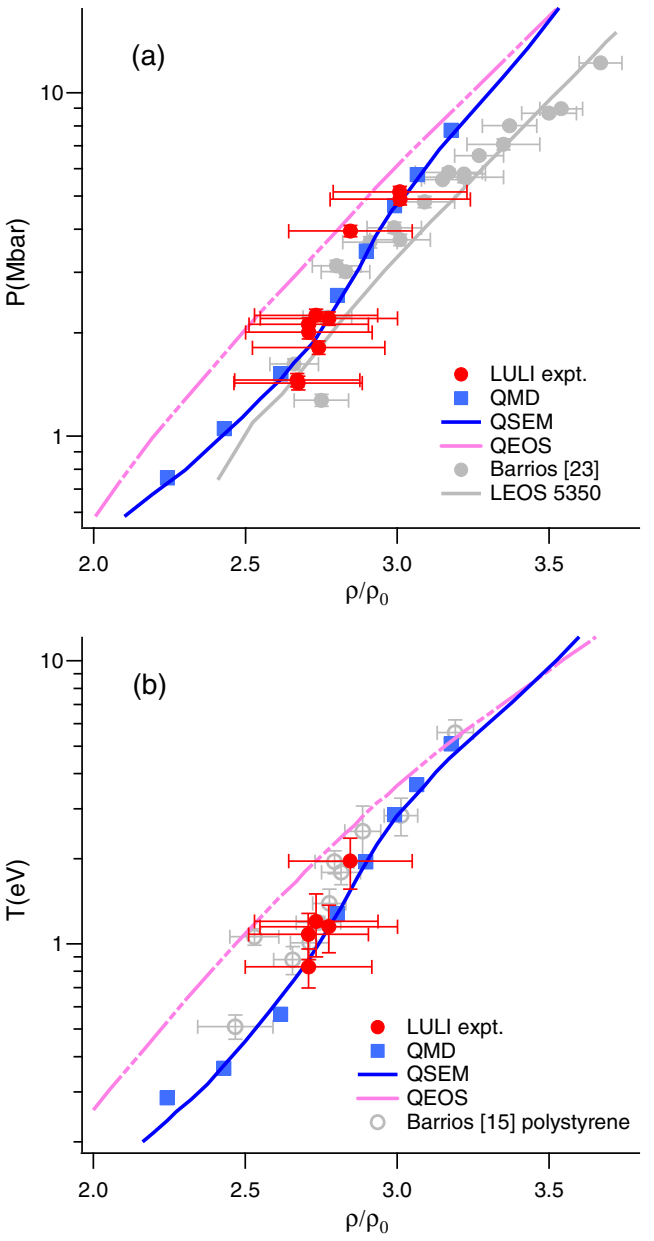

FIG. 6. GDP-CH Hugoniot data (red filled circles) in (a) pressure-compression plane and (b) temperature-compression plane, compared to the QSEM (blue line), QMD calculations (blue filled squares), and QEOS (pink dashed line). Also included are pressure-compression data for General Atomics GDP [23] (gray filled circles) and LEOS5350 (gray line, taken from Ref. [24]). Gray filled circles in temperature-compression plane (bottom graph) are polystyrene data from Ref. [15]. Data from Ref. [15] and Ref. [23] were reanalyzed using quartz standard from Ref. [45].

IV. APPLICATION TO ICF CONDITIONS

We now evaluate how this study can have an impact on integrated ICF experiments. Implosion of the capsule is obtained by a sequence of shocks of increasing strengths. This scheme minimizes entropy deposition in the cryogenic D-T fuel and is crucial in order to obtain the high densities needed for thermonuclear burn. More precisely, the shocks must travel through the cryogenic D-T following an extremely precise sequence [46] and coalesce in the gaseous D-T. If these are too close to each other, coalescence occurs in the fuel and entropy jumps to intolerable values. If the shocks are too far apart from each other, the fuel has enough time to decompress. In both cases, the D-T fuel is steered away from optimal compression. This results in extremely tight constraints on shock timing, which must be determined within 50–100 ps [20,47]. Mistiming of the shock sequence has direct consequences on the down-scattered neutrons ratio [48], which is an important observable in ICF experiments that is inversely related to fuel entropy and neutron yield [49]. Achieving such extreme precision on shock timing depends on several parameters such as laser pulse shape, resulting radiative drive in the hohlraum, and of course properties of the capsule materials such as the equation of state.

The effect of the QSEM developed in this work can readily be seen by simulating a monodimensional 500 μm thick

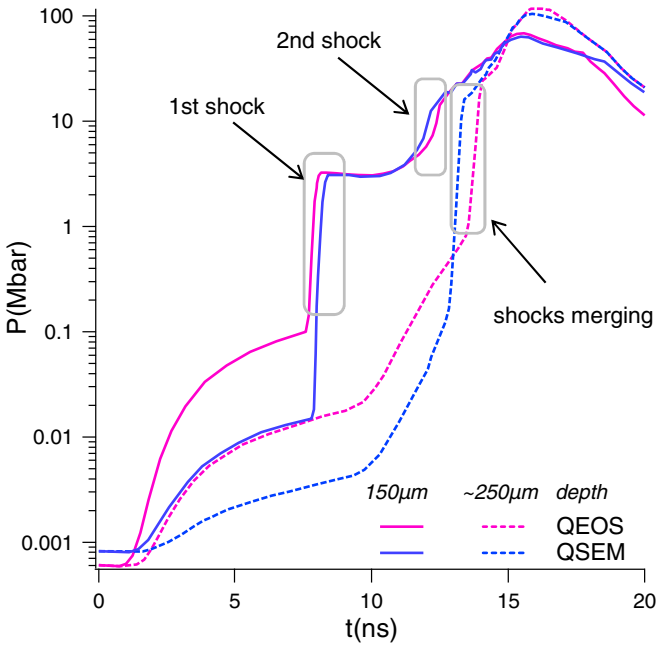

FIG. 7. CHIVAS simulations of time history of pressure in a monodimensional 500 μm thick GDP-CH slab irradiated by the radiative drive for a typical LMJ ignition design. Pressure profiles showing first and second shocks were taken at 150 μm and shock merge occur at ~250–300 μm depending on the EOS model. Color code is pink for QEOS and blue for QSEM. Continuous lines are profiles taken at 150 μm depth and dotted lines are for profiles taken at ~250–300 μm.

GDP-CH slab irradiated by the radiative drive for a typical LMJ ignition design [50]. Simulations are performed using the hydrodynamic code CHIVAS [51]. Figure 7 displays profiles of pressure history for two locations within the target, in order to show first and second shocks as well as merger of these. Simulations using QEOS and QSEM show differences in the sequences of multiple shocks. Referring to QEOS, the QSEM predicts the first shock to be ~300 ps late, the second shot to be ~300 ps early, and merger between first and second shocks to be ~600 ps early and ~20 μm closer to the outer ablator surface. This simulation provides a simplified view of the shock sequence in the ablator layer of an actual ICF capsule because the shocks actually coalesce in the D-T gas mixture, and also because convergence effects need to be taken into account. However, this basic EOS test gives a good approximation of what can be expected in a full-scale simulation. In particular, the time shifts arising from the use of two different tabulated EOSs are beyond the 50–100 ps shock timing tolerance for ignition. In the near future, a more detailed study using bidimensional simulation of a complete MJ-scale target will quantify the influence of the choice of the ablator EOS on neutron yield.

V. CONCLUSION

Using QMD simulations, we have improved our understanding of the Hugoniot behavior of GDP-CH, which is the ablator material considered for ICF capsules on the Laser Mégajoule. In particular, we have quantified the effect of atomic bond dissociation on Hugoniot compressibility. These QMD simulations, along with cold curve simulations performed in a previous work, were used to parametrize the Cowan ion EOS model within a quantum semiempirical EOS model (QSEM) in order to include the effect of dissociation. Validation of this model was given by data obtained during an experiment conducted on the LULI2000 facility, which also provided temperature data. The QSEM was tested in a monodimensional simulation and showed a strong influence on shock timing when using a radiation drive relevant to ICF conditions. Further validation of the QSEM will be needed by conducting GDP-CH Hugoniot and shock timing experiments at higher energies.

ACKNOWLEDGMENTS

We thank S. le Tacon and C. Chicanne for providing the target packages and material analysis information, M. Torrent for his help with ABINIT, and the LULI2000 laser staff for operating the laser facility.

[1] O. A. Hurricane, D. A. Callahan, D. T. Casey, P. M. Celliers, C. Cerjan, E. L. Dewald, T. R. Dittrich, T. Doppner, D. E. Hinkel, L. F. Hopkins *et al.*, Nature (London) **506**, 343 (2014).
[2] D. G. Hicks, N. B. Meezan, E. L. Dewald, A. J. Mackinnon, R. E. Olson, D. A. Callahan, T. Döppner, L. R. Benedetti, D. K. Bradley, P. M. Celliers *et al.*, Phys. Plasmas **19**, 122702 (2012).
[3] R. M. More, K. H. Warren, D. A. Young, and G. B. Zimmerman, Phys. Fluids **31**, 3059 (1988).
[4] SESAME, Tech. Rep. LA-UR-92-3407, LANL, 1992.
[5] T. R. Mattsson, J. M. D. Lane, K. R. Cochrane, M. P. Desjarlais, A. P. Thompson, F. Pierce, and G. S. Grest, Phys. Rev. B **81**, 054103 (2010).
[6] F. Lambert and V. Recoules, Phys. Rev. E **86**, 026405 (2012).
[7] D. V. Knyazev and P. R. Levashov, Phys. Plasmas **22**, 053303 (2015).
[8] C. Wang, X.-T. He, and P. Zhang, Phys. Plasmas **18**, 082707 (2011).
[9] S. X. Hu, T. R. Boehly, and L. A. Collins, Phys. Rev. E **89**, 063104 (2014).
[10] J.-F. Danel and L. Kazandjian, Phys. Rev. E **91**, 013103 (2015).
[11] S. X. Hu, L. A. Collins, V. N. Goncharov, J. D. Kress, R. L. McCrory, and S. Skupsky, Phys. Rev. E **92**, 043104 (2015).
[12] R. Cauble, L. B. D. Silva, T. S. Perry, D. R. Bach, K. S. Budil, P. Celliers, G. W. Collins, A. Ng, T. W. Barbee, Jr. *et al.*, Phys. Plasmas **4**, 1857 (1997).
[13] M. Koenig, F. Philippe, A. Benuzzi-Mounaix, D. Batani, M. Tomasini, E. Henry, and T. Hall, Phys. Plasmas **10**, 3026 (2003).
[14] N. Ozaki, T. Sano, M. Ikoma, K. Shigemori, T. Kimura, K. Miyanishi, T. Vinci, F. H. Ree, H. Azechi, T. Endo *et al.*, Phys. Plasmas **16**, 062702 (2009).

[15] M. A. Barrios, D. G. Hicks, T. R. Boehly, D. E. Fratanduono, J. H. Eggert, P. M. Celliers, G. W. Collins, and D. D. Meyerhofer, Phys. Plasmas **17**, 056307 (2010).
[16] T. Plisson, P. Colin-Lalu, G. Huser, and P. Loubeyre (unpublished).
[17] M. Stadermann, presented at 20th Target Fabrication Meeting, Santa Fe, New Mexico, May 20–24, 2012.
[18] H. Huang, D. M. Haas, Y. T. Lee, J. J. Wu, K. A. Moreno, R. B. Stephens, A. Nikroo, M. Stadermann, and S. D. Bhandarkar, Fusion Sci. Technol. **63**, 142 (2013).
[19] T. R. Boehly, V. N. Goncharov, W. Seka, S. X. Hu, J. A. Marozas, D. D. Meyerhofer, P. M. Celliers, D. G. Hicks, M. A. Barrios, D. Fratanduono *et al.*, Phys. Plasmas **18**, 092706 (2011).
[20] H. F. Robey, T. R. Boehly, P. M. Celliers, J. H. Eggert, D. Hicks, R. F. Smith, R. Collins, M. W. Bowers, K. G. Krauter, P. S. Datte *et al.*, Phys. Plasmas **19**, 042706 (2012).
[21] D. S. Clark, S. W. Haan, B. A. Hammel, J. D. Salmonson, D. A. Callahan, and R. P. J. Town, Phys. Plasmas **17**, 052703 (2010).
[22] E. Loomis, D. Braun, S. Batha, C. Sorce, and O. Landen, Phys. Plasmas **18**, 092702 (2011).
[23] M. A. Barrios, T. R. Boehly, D. G. Hicks, D. E. Fratanduono, J. H. Eggert, G. W. Collins, and D. D. Meyerhofer, J. Appl. Phys. **111**, 093515 (2012).
[24] S. Hamel, L. X. Benedict, P. M. Celliers, M. A. Barrios, T. R. Boehly, G. W. Collins, T. Döppner, J. H. Eggert, D. R. Farley, D. G. Hicks *et al.*, Phys. Rev. B **86**, 094113 (2012).
[25] The ABINIT code is a common project of the Université Catholique de Louvain, Corning Incorporated, Université de Liège, Commissariat à l'Energie Atomique, Mitsubishi Chemical Corp., and the Ecole Polytechnique Palaiseau; see http://www.abinit.org.
[26] X. Gonze, B. Amadon, P.-M. Anglade, J.-M. Beuken, F. Bottin, P. Boulanger, F. Bruneval, D. Caliste, R. Caracas, M. Côté *et al.*, Comput. Phys. Commun. **180**, 2582 (2009).
[27] F. Bottin, S. Leroux, A. Knyazev, and G. Zérah, Comput. Mater. Sci. **42**, 329 (2008).
[28] J. P. Perdew, K. Burke, and M. Ernzerhof, Phys. Rev. Lett. **77**, 3865 (1996).
[29] P. E. Blöchl, Phys. Rev. B **41**, 5414 (1990).
[30] M. Torrent, F. Jollet, F. Bottin, G. Zérah, and X. Gonze, Comput. Mater. Sci. **42**, 337 (2008).
[31] P. Colin-Lalu, V. Recoules, G. Salin, and G. Huser, Phys. Rev. E **92**, 053104 (2015).
[32] R. Piron and T. Blenski, Phys. Rev. E **83**, 026403 (2011).
[33] D. A. Liberman, J. Quant. Spectrosc. Radiat. Transfer **27**, 335 (1982).
[34] J. F. Barnes, Phys. Rev. **153**, 269 (1967).
[35] Y. B. Zel'dovich and Y. P. Raizer, *Physics of Shock Waves and High-Temperature Hydrodynamic Phenomena* (Academic, New York, 1967).
[36] M. J. L. Sangster, G. Peckham, and D. H. Saunderson, J. Phys. C **3**, 1026 (1970).
[37] N. Vocadlo and G. D. Price, Phys. Earth Planet. Inter. **82**, 261 (1994).
[38] D. A. Young and E. M. Corey, J. Appl. Phys. **78**, 3748 (1995).
[39] D. G. Hicks, T. R. Boehly, P. M. Celliers, J. H. Eggert, E. Vianello, D. D. Meyerhofer, and G. W. Collins, Phys. Plasmas **12**, 082702 (2005).
[40] M. D. Knudson, M. P. Desjarlais, and A. Pribram-Jones, Phys. Rev. B **91**, 224105 (2015).
[41] See http://web.luli.polytechnique.fr/Neutrino.
[42] L. V. Al'tshuler, S. B. Kormer, M. I. Brazhnik, L. Vladimirov, M. P. Speranskaya, and A. I. Funtikov, Sov. Phys. JETP **38**, 1061 (1960).
[43] D. G. Hicks, T. R. Boehly, J. H. Eggert, J. E. Miller, P. M. Celliers, and G. W. Collins, Phys. Rev. Lett. **97**, 025502 (2006).
[44] G. Huser, V. Recoules, N. Ozaki, T. Sano, Y. Sakawa, G. Salin, B. Albertazzi, K. Miyanishi, and R. Kodama, Phys. Rev. E **92**, 063108 (2015).
[45] M. D. Knudson and M. P. Desjarlais, Phys. Rev. B **88**, 184107 (2013).
[46] D. H. Munro, P. M. Celliers, G. W. Collins, D. M. Gold, L. B. Da Silva, S. W. Haan, R. C. Cauble, B. A. Hammel, and W. W. Hsing, Phys. Plasmas **8**, 2245 (2001).
[47] O. L. Landen, J. Edwards, S. W. Haan, H. F. Robey, J. Milovich, B. K. Spears, S. V. Weber, D. S. Clark, J. D. Lindl, B. J. MacGowan *et al.*, Phys. Plasmas **18**, 051002 (2011).
[48] H. F. Robey, B. J. MacGowan, O. L. Landen, K. N. LaFortune, C. Widmayer, P. M. Celliers, J. D. Moody, J. S. Ross, J. Ralph, S. LePape *et al.*, Phys. Plasmas **20**, 052707 (2013).
[49] M. J. Edwards, J. D. Lindl, B. K. Spears, S. V. Weber, L. J. Atherton, D. L. Bleuel, D. K. Bradley, D. A. Callahan, C. J. Cerjan, D. Clark *et al.*, Phys. Plasmas **18**, 051003 (2011).
[50] C. Cherfils-Clérouin, C. Boniface, M. Bonnefille, E. Dattolo, D. Galmiche, P. Gauthier, J. Giorla, S. Laffite, S. Liberatore, P. Loiseau *et al.*, Plasma Phys. Controlled Fusion **51**, 124018 (2009).
[51] A. Decoster (private communication).